High figure-of-merit of $Mg_{1.96}Zn_{0.04}(Si_{0.3}Sn_{0.7})_{0.98}Sb_{0.02}$ alloy through simultaneous optimization of electrical and thermal transports

Pritam Sarkar[1,2], Pankaj Gupta[3], U. Sandhya Shenoy[4], Surjeet Singh[3], Sayandeep Kundu[5], Nitin Kumawat[6], Dinesh Kedia[3], D. Krishna Bhat[7], Shovit Bhattacharya[1,2], Ajay Singh[1,2*]

[1]*Homi Bhabha National Institute, Anushaktinagar, Mumbai-400085, India*
[2]*Technical Physics Division, Bhabha Atomic Research Centre, Mumbai-400085, India*
[3]*Indian Institute of Science Educations and Research, Pune, India*
[4]*Department of Materials Science and Engineering, Institute of Engineering and Technology, Srinivas University, Mukka, Mangalore - 574146, Karnataka, India*
[5]*Atomic Fuels Division, Bhabha Atomic Research Centre, Mumbai-400085, India*
[6]*Post Irradiation Examination Division, Bhabha Atomic Research Centre, Mumbai-400085, India*
[7]*Department of Chemistry, National Institute of Technology Karnataka, Surathkal, Mangalore – 575025*

**Corresponding author: Ajay Singh (Email: ajay@barc.gov.in)*

Preprint not peer reviewed

This preprint research paper has not been peer reviewed. Electronic copy available at: https://ssrn.com/abstract=5179051

Graphical abstract

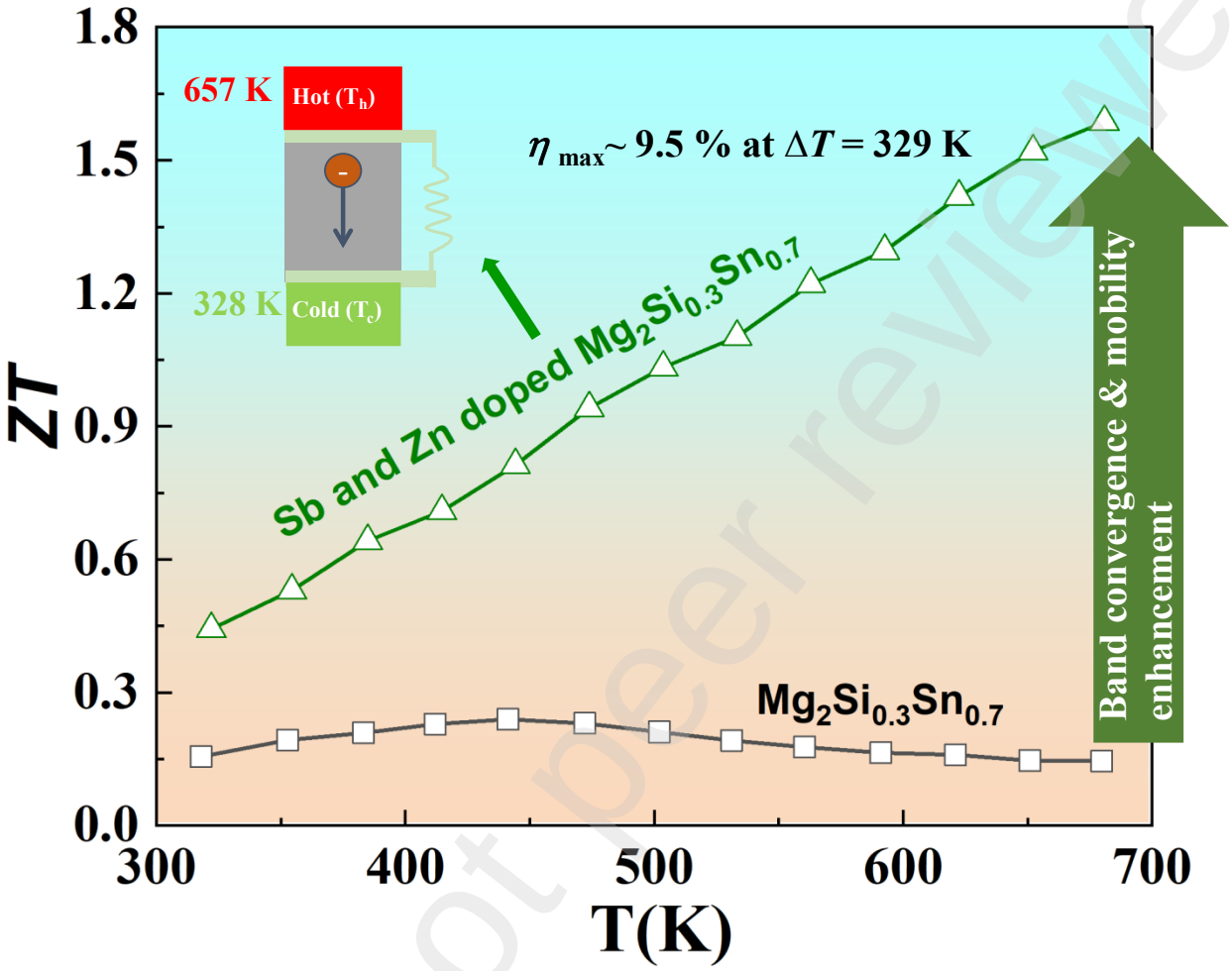

Highlight

1: Simultaneous boosting of electrical conductivity and Seebeck coefficient in $Mg_{1.96}Zn_{0.04}(Si_{0.3}Sn_{0.7})_{0.98}Sb_{0.02}$ achieved through the hyper-convergence in the conduction band.

2: The doping induced point defects and dislocations decrease $\kappa_{lattice}$, resulting in high ZT of ~ 1.6 and $(ZT)_{eng}$ ~0.7 at 673 K in $Mg_{1.96}Zn_{0.04}(Si_{0.3}Sn_{0.7})_{0.98}Sb_{0.02}$.

3: Uni-leg device of $Mg_{1.96}Zn_{0.04}(Si_{0.3}Sn_{0.7})_{0.98}Sb_{0.02}$ showed impressive efficiency of ~ 9.5 % at ΔT ~ 329 K.

Preprint not peer reviewed

This preprint research paper has not been peer reviewed. Electronic copy available at: https://ssrn.com/abstract=5179051

Abstract

The derivatives of Mg_2Si have recently attracted wide attention as promising thermoelectric materials due to earth abundant and environment friendly low-cost constituents. The main challenge in optimizing the thermoelectric figure of merit *ZT*, is the low electrical and high thermal conductivities of Mg_2Si. The present study demonstrates high *ZT* of ~ 1.6 at 673 K in $Mg_2Si_{0.3}Sn_{0.7}$ through simultaneous optimization of electrical and thermal transport through Sb and Zn co-doping. The ultra-low deformation and alloy scattering potentials in Sb and Zn co-doped samples helps in maintaining record high Hall mobility ~ 70-90 $cm^2/V.s$. The doping induced pudding mold band structure with hyperconvergence in conduction band balances high Seebeck coefficient and high electrical conductivity. The point defects and dislocations created by doping helps in lowering of lattice thermal conductivity as well. The uni-leg power generator fabricated using optimized $Mg_{1.96}Zn_{0.04}(Si_{0.3}Sn_{0.7})_{0.98}Sb_{0.02}$ exhibits a record efficiency of ~ 9.5 % at ΔT ~ 329 K.

Preprint not peer reviewed

This preprint research paper has not been peer reviewed. Electronic copy available at: https://ssrn.com/abstract=5179051

Introduction

The ever-increasing demand of energy and impending crisis of global warming related to increasing use of fossil fuel has forced mankind to arrange for alternative energy source as well as reduction in waste heat. Thermoelectric materials are ideal for direct conversion of waste heat into electricity. The conversion efficiency of a thermoelectric material mainly depends upon the dimensionless figure of merit $ZT = \alpha^2\sigma T/\kappa$ where α is the Seebeck coefficient, σ is the electrical conductivity and κ is the total thermal conductivity having lattice (κ_L), electronic (κ_e) and bipolar (κ_b) contributions. However, these parameters are adversely interdependent and decoupling them for the betterment of overall *ZT* is an extremely challenging task. The numerator part of *ZT* i.e. $\alpha^2\sigma$ is called power factor (PF) and it is relatively less dependent on κ_L. The various strategies were evolved to enhance *ZT* includes optimization of carrier concentration[1], increasing effective mass via band convergence[2, 3], introduction of resonant levels[2, 4, 5] , band structure engineering[6, 7, 8, 9, 10], hyperconvergence of bands[11], introduction of multiple electron valleys[12], pudding mold band features[13], Rashba splitting[14], decreasing κ_L by defect engineering[15] etc. Apart from *ZT*, the thermoelectric quality factor *B* is an indicator of the efficiency of material[16]. According to Bardeen and Shockley[16-17] *B* is defined as:

$$B = \frac{2\hbar C_l N_v k_B^2 T}{3\pi m_I^* \kappa_L {E_{def}}^2} \quad (1)$$

Where k_B is the Boltzmann constant, ħ is the reduced Plank constant, C_l is the longitudinal elastic constant, *Nv* is the valley band degeneracy, m_I^* is the inertial effective mass and E_{def} is the deformation potential. Evidently, a high N_v, low κ_L and low E_{def} are preferred to maximize *B*. Moreover, as electronic and lattice part of *ZT* are assumed to be independently tunable, Slack proposed the idea of weighted mobility (μ_w) [18] which governs the goodness of the electronic part of a material and is defined as[16]:

Preprint not peer reviewed

This preprint research paper has not been peer reviewed. Electronic copy available at: https://ssrn.com/abstract=5179051

$$\mu_w = \mu_0 \left(\frac{m^*}{m_e}\right)^{\frac{3}{2}} \quad (2)$$

Where μ_0 is the mobility in the purest defect free (undoped) material[16] where carrier concentration is negligible and m^* is the density of state effective mass. By combining the electronic and lattice part of a thermoelectric material another parameter β is defined as $(m^*/m_e)^{3/2}\mu_0/\kappa_L$, which is also used as a signature of a good thermoelectric material[19].

Most of the high-performance thermoelectric materials (e.g. PbTe, Bi_2Te_3, SiGe etc) usually contain expensive or toxic elements. In this regard, Mg_2B^{XIV} (B^{XIV} = Si, Ge, and Sn) and their solid solutions, specially $Mg_2Si_{1-z}Sn_z$ (z = 0.4 – 0.7), synthesized from non-toxic, naturally abundant constituent elements, demonstrate impressive thermoelectric properties and low mass density along with good mechanical properties. $Mg_2Si_{1-x}Sn_x$ (x ~ 0.6 – 0.7) shows good thermoelectric properties[19b], [20], [21], [22] because of increased m^* as two electronic bands converges increasing valley degeneracy N_v = 3 to 6, decoupling adverse dependence between Seebcek coefficient and electrical conductivity. Moreover, due to mass mismatch among atoms and introduction of strain the thermal conductivity gets reduced. However the mass mismatch and strain can also scatter charge carriers and thus can reduce mobility[23]. The estimation of alloy scattering potential E_{alloy} gives an indication of the effect of alloying on the mobility of electrical transport[24]. Deformation potential E_{def} and alloy scattering potential E_{alloy} are the two key factors that decide carrier mobility (μ) in a solid solution or alloy[25]. E_{def} characterizes scattering of carriers by lattice vibration which is basically coupling between phonons and electrons and alloy scattering potential E_{alloy} signifies interaction of carriers with the potential fluctuations due to atomic disorder in alloys or solid solutions[17], [26].

In this work we investigate the thermoelectric properties of Sb doped carrier concentration optimized $Mg_2Si_{0.3}Sn_{0.7}$ showing a record ZT of ~ 1.55 at 673 K due to very high Hall mobility ~ 70 cm^2/Vs. We further investigate the role of Zn substitution at Mg site in $Mg_{2(1-}$

Preprint not peer reviewed

This preprint research paper has not been peer reviewed. Electronic copy available at: https://ssrn.com/abstract=5179051

$_{x)}Zn_{2x}(Si_{0.3}Sn_{0.7})_{0.98}Sb_{0.02}$ and it was found that ~ 2 atomic% Zn doping reaches its solubility limit and above this limit it gets segregated into the matrix thus creating vacancy at cationic sites and introducing bipolar conduction. To the best of our knowledge the role of Zn doping is not much investigated in detail for $Mg_2Si_{0.3}Sn_{0.7}$[27], [28] . Though, earlier[27] it is reported that Zn doping in $Mg_2Si_{0.3}Sn_{0.7}$ improves mobility without much insight of such an observation. In this work we concussively demonstrate that Zn doping leads to ultra-low E_{def} $(8.0 - 8.1\ \text{eV})$ and E_{alloy} (0.3 - 0.31 eV) and it agrees with the DFT calculated band structure.

Experimental and computational details:

For synthesis of $Mg_{2(1-x)}Zn_{2x}(Si_{0.3}Sn_{0.7})_{1-y}Sb_y$ (x = 0, 0.01, 0.02, 0.03 & y = 0, 0.02), Mg metal turning (99.9%, Arrobiochem make), Pulverized Si powder in agate mortar pestle from Silicon lump (99.9999%, 0.1-2.5 cm, Alfa Aesar make), Pulverized Sb powder in agate mortar pestle Sb shots (99.9999%, 1-3 mm, Alfa Aesar make), Zn ingots (99.99%, NFC make) were taken stoichiometrically and cold pressed. The cold pressed cylindrical green pellets were taken inside an air tight graphite crucible with inner walls tapered with Boron Nitride (BN) solution. The crucible was then heated to 1000˚ C for 10 mins in an induction furnace in presence of Argon gas (~ 0.6 atm. pressure). To compensate for Mg loss at high temperature, 5 atomic % extra Mg were taken for each sample. After melting, these ingots were pulverized in fine powder in a mortar pestle and then hot pressed in the same induction furnace in a graphite die of dia. ~ 10 mm under 440 kg load for 7 min in presence of Argon gas (~ 0.6 atm. pressure). The hot-pressed pellets of dia. ~ 10 mm, height ~ 1.5-2 mm were used for measurement of thermal conductivity. Rectangular bars (10 mm × 5 mm × 4 mm) and thin slices (0.67 mm × 9.8 mm × 10 mm) were cut from the hot-pressed pellet of dia.: 10 mm, height ~ 10-11 mm using diamond coated wheel for electrical transports and Hall coefficient measurement, respectively. The relative densities of all the samples were ~ 97-99%.

Preprint not peer reviewed

This preprint research paper has not been peer reviewed. Electronic copy available at: https://ssrn.com/abstract=5179051

The crystal structure was characterized using X-Ray powder diffraction technique (XRD, Proto make Benchtop Powder Diffraction System) at room temperature with Cu K_α radiation. Rietveld Refinement is done using Fullprof software. The simultaneous measurement of temperature dependent Seebeck coefficient and electrical conductivity were done on rectangular bar shaped samples using an LSR3 setup (Linseis make). The maximum uncertainty in these measurements is 5%. The thermal conductivity κ was calculated using $\kappa = D\rho C_p$, where ρ is the experimentally measured sample density, C_p is the specific heat estimated using Dulong Petit's law and D (thermal diffusivity) was measured using the laser flash method (LFA 1000, Linseis). The temperature dependent Hall measurements were performed in a homebuilt setup under a dynamic vacuum. The setup maintains temperature stability better than 10 mK. A phase-sensitive lock-in technique and electromagnetic shielding allow for precise measurements of our samples with Hall voltage in the nanovolts range. For probing, stainless-steel pressure-point contacts were used on hall-bar geometry samples. The Hall voltage is obtained as $V_H(H) = (V_m(+H)-V_m(-H))/2$. To evaluate the Hall carrier concentration (n_H), we use $R_H=1/(n_He) = V_Ht/(IH)$, where V_H/H is obtained from the slope of the Hall data, I is the probe current, and t is the sample thickness. The microstructure and elemental distribution were assessed using the field effect scanning electron microscopy (FESEM, Carl Zeiss Gemini SEM 300) equipped with Energy Dispersive X-ray Spectroscopy (EDS, Oxford Instruments 100 mm^2 detector, EDS Ultim 100). EDS data were analyzed using AZtec software. Sound velocity in the samples (h ~ 1 cm, Φ ~ 1 cm) were measured using GE Make USN 60L, Olympus make probe of 4 MHz, 6 mm diameter and 2.25 MHz, 12 mm diameter for longitudinal and transverse velocities respectively. The high-resolution electron micrographs were obtained using a transmission electron microscope (JEOL JEM 2200FS 200 keV). The first-principles calculations were performed within the framework of density functional theory (DFT) using Quantum ESPRESSO package[29]. Generalized gradient approximation (GGA) of Perdew−Burke−Ernzerhof (PBE) functional type was employed to

Preprint not peer reviewed

This preprint research paper has not been peer reviewed. Electronic copy available at: https://ssrn.com/abstract=5179051

describe the exchange-correlation potential[30]. A conventional cell was used for the simulation of the face centered cubic crystal with $2s^2\ 2p^6\ 3s^2$, $3s^2\ 3p^2$, $4d^{10}\ 5s^2\ 5p^2$, $4d^{10}\ 5s^2\ 5p^3$, $3d^{10}\ 4s^2$ as valence electrons for Mg, Si, Sn, Sb and Zn atoms. While Sn and Sb atoms were substituted at Si site, Zn atom was substituted at Mg site in the doped samples. Plane wave basis was used to represent the wave functions, the energy and charge density of which were terminated using 50 Ry and 400 Ry respectively. A k-mesh of 12×12×12 points was used to sample the Brillouin zone integrations. The electronic structures were determined along Γ-X-M-Γ-R-X path for the fully relaxed chosen cell. In the later part of manuscript the un-doped sample $Mg_2Si_{0.3}Sn_{0.7}$ is termed as S1 while doped samples $Mg_{2(1-x)}Zn_{2x}(Si_{0.3}Sn_{0.7})_{0.08}Sb_{0.02}$ (x = 0, 0.01, 0.02, 0.03) are termed as S2, S3, S4 and S5.

Results and Discussion:

The XRD patterns of $Mg_{2(1-x)}Zn_{2x}(Si_{0.3}Sn_{0.7})_{1-y}Sb_y$ (x = 0, 0.01, 0.02, 0.03 & y = 0, 0.02) samples are shown in Figure 1. All other major diffraction peaks in Figure 1. (a) can be indexed with antifluorite crystal structure ($Fm\bar{3}m$ space group, ICSD Coll. Code: 671458). It is important to mention that contrary to previous studies the diffraction peaks corresponding to MgO are negligibly small in our samples. The absence of MgO is beneficial to obtain high mobility as MgO is an insulator and its segregation at the grain boundaries hampers the facile transport of charge carriers[31].

Preprint not peer reviewed

This preprint research paper has not been peer reviewed. Electronic copy available at: https://ssrn.com/abstract=5179051

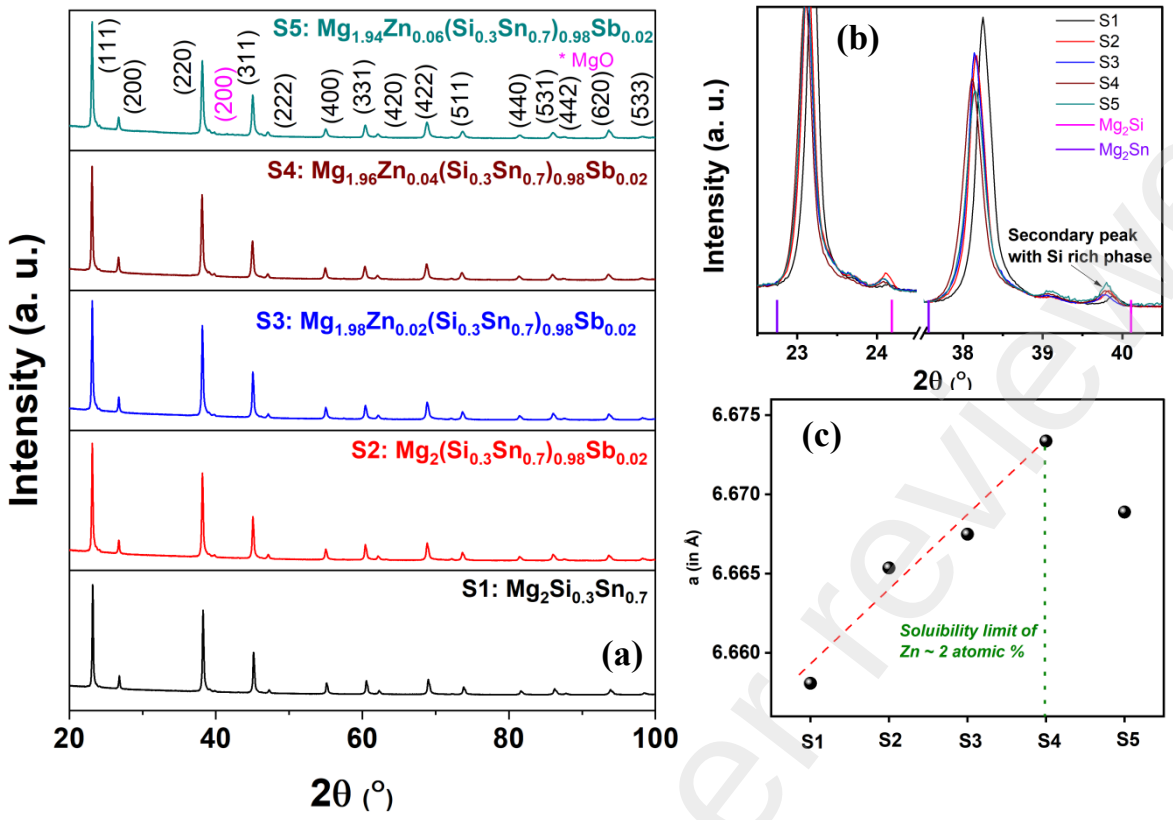

Fig. 1. (a) XRD data of $Mg_{2(1-x)}Zn_{2x}(Si_{0.3}Sn_{0.7})_{1-y}Sb_y$ (x = 0, 0.01, 0.02, 0.03 & y = 0, 0.02) samples, (b) Zoomed neighborhood of (111) and (220) peak indicating presence minor secondary Si rich phases, (c) Calculated lattice constant with sample code. Up to ~ 2 atomic% doping, Zn is soluble in the matrix and expands the lattice constant. Above this limit, Zn starts segregating in the matrix.

In the XRD data very low intensity diffraction peaks corresponding to Si rich phases (Figure 1. (b)) are also seen, which is later supported by the X-ray elemental mapping images of samples. The formation of such Si rich phases is inherent since the miscibility gap exist in phase diagram of solid solution of Mg_2Si-Mg_2Sn [32]. Such secondary Si or Sn rich phases in $Mg_2Si_{1-z}Sn_z$ (z = 0.4 – 0.7) alloys are also previously reported [22], [32a], [33], [34], [35] . It is also reported that such Si rich phases does not have any influence the thermoelectric transport properties. Another interesting feature seen in Figure. 1(c) is that up to 2 atomic % Zn doping XRD peaks shift towards lower 2Θ indicating expansion of lattice [27-28]. As seen from Figure 2 (c), above this limit the lattice starts shrinking, indicating the solubility limit of Zn is up to ~ 2 atomic %. Such

Preprint not peer reviewed

This preprint research paper has not been peer reviewed. Electronic copy available at: https://ssrn.com/abstract=5179051

a shrink of lattice parameter at high Zn content (> 2 atomic %) is attributed to Mg vacancies as well as due to limited solubility of Zn in the S5 sample. Usually during synthesis of $Mg_2Si_{0.3}Sn_{0.7}$ samples at high temperature, Mg loss occurs. Hence extra Mg (optimized by trial-and-error method) is taken from the beginning of the synthesis to compensate for Mg loss. The amount of Mg loss may vary in different experimental synthesis setup. For our case we have optimised that 5 atomic % extra Mg needs to be taken for all samples to compensate the Mg loss. This extra Mg if goes at the interstitial position (Mg_i), increase the carrier concentrations [36] thus increasing the electrical conductivity. Du et. al. has systemically varied the amount of extra Mg [36] and found that the disorder in the crystal structure due to presence of Mg_i increases the FWHM of (*111*) diffraction peak. The low FWHM for the samples reported in present work (Figure 2) signifies lesser concentration of Mg_i donor defects as compared to the reported ones [36] hence not affecting the carrier concentration.

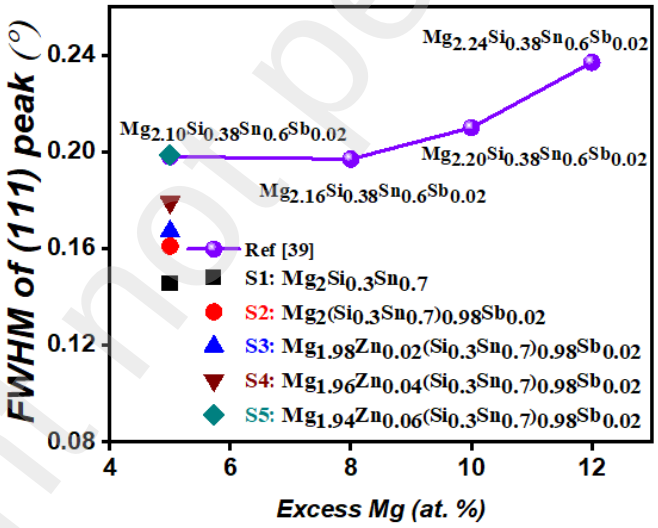

Fig. 2. Comparison of the FWHM of (*111*) diffraction peak reported by Du. Et. al [36] with the present work. In our samples S1-S5, 5 atomic% extra Mg was taken in each sample.

The temperature dependent electrical conductivity for all samples is shown in Figure 2. (a). The electrical conductivity of undoped S1: $Mg_2(Si_{0.3}Sn_{0.7})$ increases with rising temperature

Preprint not peer reviewed

This preprint research paper has not been peer reviewed. Electronic copy available at: https://ssrn.com/abstract=5179051

suggesting intrinsic conduction due to very low carrier concentration (n_H ~ 5.2 × 10^{18}/cm^3 at 300 K estimated using Hall measurement). With Sb doping the carrier concentration increases to 2.96 × 10^{20}/cm^3 in Sb doped sample S2: $Mg_2(Si_{0.3}Sn_{0.7})_{0.98}Sb_{0.02}$. The electrical conductivity for sample S2 decreases with increasing temperature indicating the character of a degenerate semiconductor. Now in next set of samples (S3-S5) we have fixed Sb doping at 2 atomic % and Zn doping is done at Mg site. Since Zn is isoelectronic to Mg and hence it should not change carrier concentration [27]. The Hall measurement data shown in Figure 3(a) suggest that up to 2 atomic % of Zn doping at Mg site n_H remains nearly same ~ 2.4 -2.67 ×10^{20}/ cm^3 and 2.40 × 10^{20}/ cm^3 for S3: $Mg_{1.98}Zn_{0.02}(Si_{0.3}Sn_{0.7})_{0.98}Sb_{0.02}$ and S4: $Mg_{1.96}Zn_{0.04}(Si_{0.3}Sn_{0.7})_{0.98}Sb_{0.02}$ respectively at 300 K. All these samples show decreasing trend of electrical conductivity with increasing temperature indicating highly doped degenerate semiconductor nature. As seen from the information revealed by the XRD data of Fig. 1(c), the Zn has a limited solubility up to 2 atomic % at Mg site. Hence in S5 sample (with Zn content ~ 3 atomic %) the vacancies at Mg sites (V_{Mg}) can exist, which act as acceptors doping[19b] . The reduced carrier concentration (n_H ~ 1.65 × 10^{19}/cm^3 at 300 K) in S5: $Mg_{1.94}Zn_{0.06}(Si_{0.3}Sn_{0.7})_{0.98}Sb_{0.02}$ support that existence of V_{Mg} in the sample and as seen from Figure 3(a), the temperature dependent electrical conductivity for S5 sample shows increasing trend at high temperature supporting intrinsic conduction in the sample.

The temperature dependence of Seebeck coefficient for all samples are plotted in Fig. 3. (b). The negative Seebeck coefficient of all samples indicates the expected n-type conduction and electron as the majority charge carriers. For the Sb undoped S1: $Mg_2(Si_{0.3}Sn_{0.7})$, Seebeck coefficient starts decreasing at high temperature (~450 K) due to onset of bipolar conduction.

Preprint not peer reviewed

This preprint research paper has not been peer reviewed. Electronic copy available at: https://ssrn.com/abstract=5179051

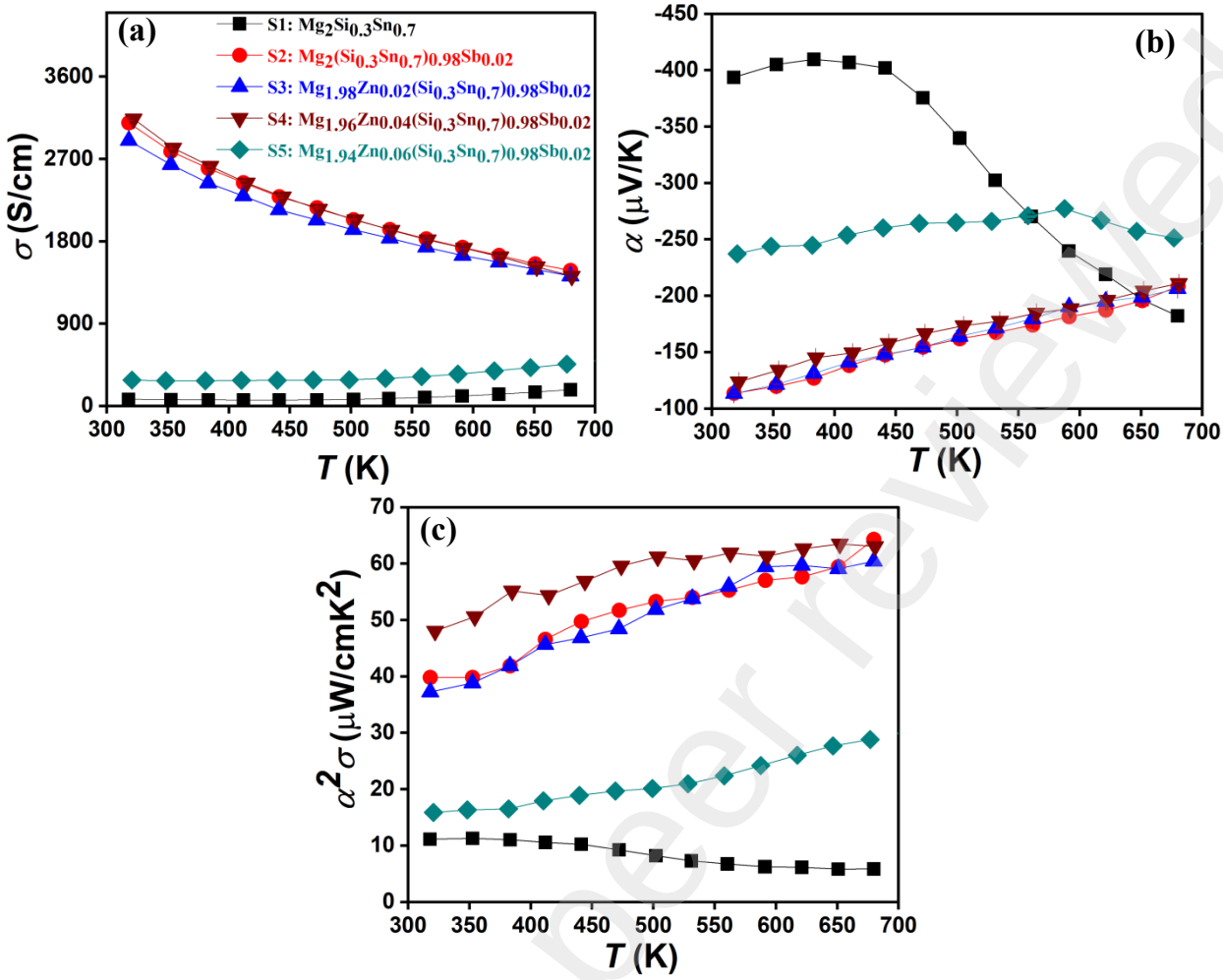

Fig. 3. Temperature dependent thermoelectric properties of $Mg_{2(1-x)}Zn_{2x}(Si_{0.3}Sn_{0.7})_{1-y}Sb_y$ (x = 0, 0.01, 0.02, 0.03 & y = 0, 0.02) samples: (a) Electrical conductivity, (b) Seebeck coefficient, (c) Power Factor.

As expected in Sb doped S2, S3, S4 samples bipolar effect gets suppressed due to enhanced extrinsic carrier concentration and as a result the Seebeck coefficient keeps on increasing in the temperature range of 323 – 673 K [Fig. 3. (b)]. Moreover, the absolute value of Seebeck coefficient decreases in S2-S4 compared to S1 because of their higher carrier concentration. To understand the change of conduction nature from extrinsic to intrinsic for all our samples high temperature Hall measurements were carried out and results are plotted in Figure 4 (a). For S2, S3, S4, a rather weak temperature dependence of carrier concentration (n_H) over 300 K-660 K confirms the extrinsic nature of conduction which agrees with the temperature dependence of

Preprint not peer reviewed

This preprint research paper has not been peer reviewed. Electronic copy available at: https://ssrn.com/abstract=5179051

Seebeck coefficient and electrical conductivity. For S1 and S5, n_H increases at high temperature confirming onset of bipolar conduction. For S2, S3, S4 the n_H (at 300 K) is nearly constant with a value in the range of ~ 2.4 – 2.9 $\times 10^{20}$, which is close to optimized carrier concentration for the reported sample [15, [21], 17, [37]]. Zhu. Et. al. [32b] plotted the expected linear relationship between the n_H and the Sb/Bi doping concentration, assuming dopant atoms are solely responsible for extrinsic carrier concentration. The Fig. 4. (b) shows the report data on n_H versus Sb/Bi doping concentration and we have compared our results with the reported literature(s) [20], [36], [19b, 22, 27, 34, 38]. We note that n_H of our samples lies closely to the predicted theoretical data. Since the samples prepared in this work shows excellent density (~ 97-99% of theoretical density ~ 3.2 gm/c.c.) therefore it can be concluded that Mg_i is minimal in our samples which corroborates the findings from FWHM of XRD peaks shown in Fig 2 as well.

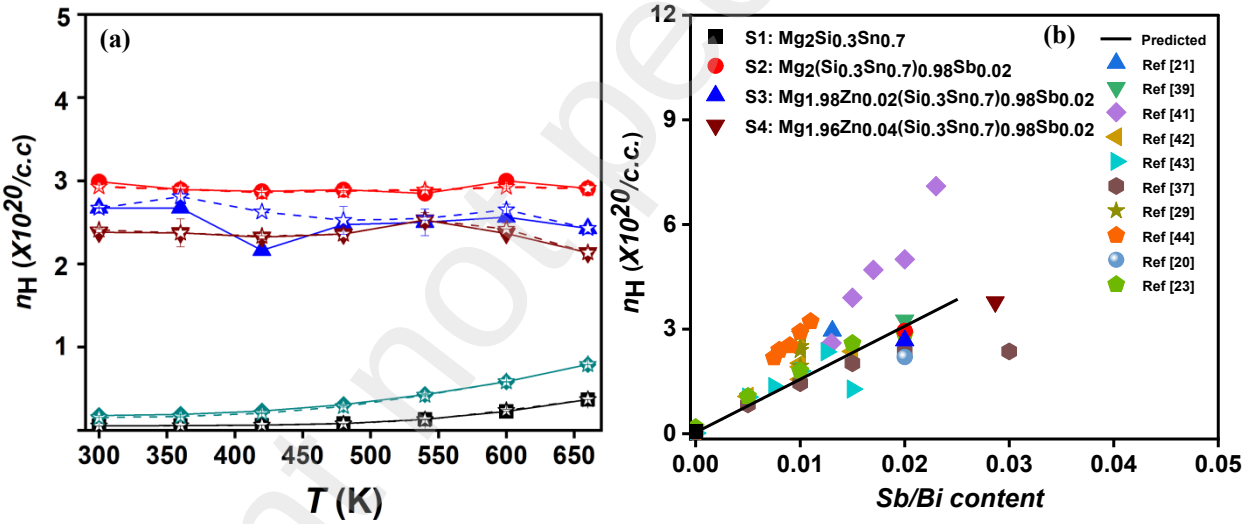

Fig. 4. (a) Plot of n_H vs T of all samples. The continuous and dashed line connects n_H obtained during heating (filled markers) and cooling (unfilled star symbols) respectively. (b) Theoretical prediction of expected n_H with Sb/Bi doping assuming Sb/Bi is the sole electron donator. Our sample remains close to this line when compared to literature.

In the Pisarenko plot of α vs n_H [Fig. 5] it can be directly observed that the density of state effective mass m^* for S2, S3 and S4 is ~ 2.7-2.55 m_e and shows good agreement between

This preprint research paper has not been peer reviewed. Electronic copy available at: https://ssrn.com/abstract=5179051

experimental data and theoretically calculated curves using Single Parabolic Band (SPB) model, both at 300 K and 600 K. This essentially indicates temperature independent density of state effective mass, at different carrier concentrations[20, 25], in the temperature range of interest (300 K – 673 K). Comparing the Seebcek coefficient in Sb doped Mg_2Si or Mg_2Sn[19b, 20, 37] with our Sb/Zn doped samples, it can be concluded that band convergence is taking place and as a result high m^* is observed even at same carrier concentration[10],[20],[22]. Moreover, the high m^* along with its temperature independence in Sb/Zn doped $Mg_2Si_{0.3}Sn_{0.7}$ ensures high Seebeck coefficient from 300 K to 660 K with stable band structure unlike temperature dependent band convergence seen in some of the thermoelectric materials like $PbTe_{1-x}Se_x$[20] or Mg_2Ge[39]. This high Seebeck coefficient along with excellent high electrical conductivity (2900~3100 S/cm at 323 K) in our Sb and Zn doped $Mg_{1.96}Zn_{0.04}(Si_{0.3}Sn_{0.7})_{0.98}Sb_{0.02}$ result in extraordinarily high power factor ~ 35-45 $\mu W/cmK^2$ at 323 K and ~ 57-61 $\mu W/cmK^2$ at ~ 600 K, which is significantly higher than the previously reported values[21],[22]. To gain further insight of the electrical transports characteristics, results have been analyzed using single parabolic band (SPB) model which assumes that the converged bands can be treated as a single parabolic rigid band with the following assumptions: the density of state effective mass is carrier concentration independent and the band structure remains unchanged upon dopant substitution.

Preprint not peer reviewed

This preprint research paper has not been peer reviewed. Electronic copy available at: https://ssrn.com/abstract=5179051

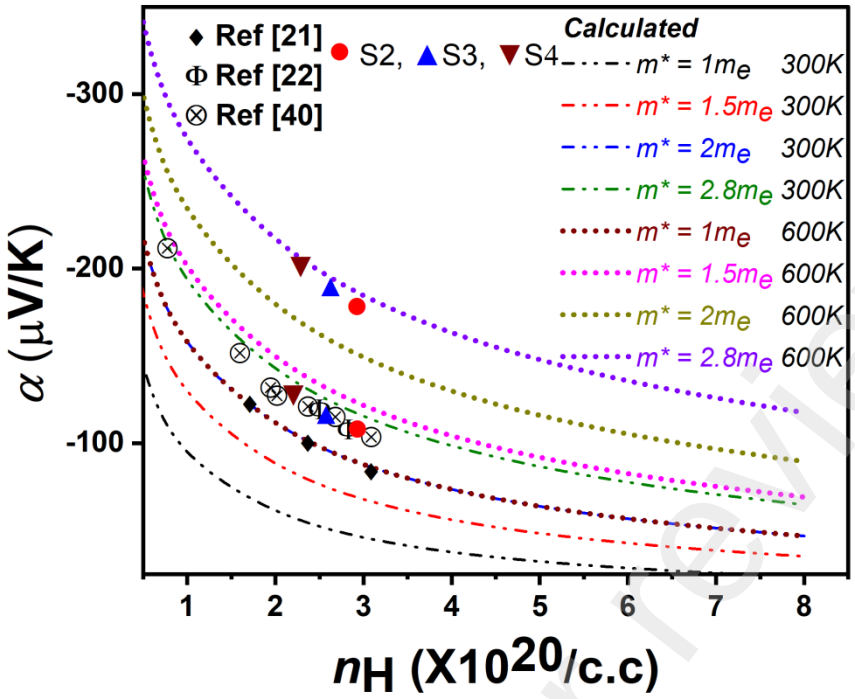

Fig. 5. (a) Pisarenko plot of α vs n_{H} with m^* as fitting parameter. The dotted line represents theoretically calculated curve using SPB model and our samples S2, S3 and S4 are compared with the literature reported values.

SPB is governed by the following set of equations:

$$\alpha = \frac{k_B}{e}\left[\frac{2F_1(\eta)}{F_0(\eta)} - \eta\right], F_j(\eta) = \int_0^\infty \frac{x^j dx}{1 + exp\,(x-\eta)}, \eta = \frac{E_F}{k_B T} \tag{3}$$

$$r_{\mathrm{H}} = \frac{3}{4}\frac{F_{0.5}(\eta)F_{-0.5}(\eta)}{F_0^2(\eta)} \tag{4}$$

$$\sigma = \frac{\mu_{\mathrm{H}}}{R_{\mathrm{H}}}\ , n = r_{\mathrm{H}} n_{\mathrm{H}}, \mu_{\mathrm{H}} = \mu_0 \frac{F_{-0.5}(\eta)}{2F_0\,(\eta)} \tag{5}$$

$$n = 4\pi\left(\frac{2m^* k_B T}{h^2}\right)^{\frac{3}{2}} F_{0.5}(\eta) \tag{6}$$

Preprint not peer reviewed

This preprint research paper has not been peer reviewed. Electronic copy available at: https://ssrn.com/abstract=5179051

$$L = \left(\frac{k_B}{e}\right)^2 \left(\frac{3F_0(\eta)F_2(\eta) - 4F_1^2(\eta)}{F_0^2(\eta)}\right) \quad (7)$$

where $F_j(\eta)$ is the Fermi integral of j-th order, η is reduced Fermi energy, r_H is hall factor, $R_H = -(1/n_H e)$ is the Hall coefficient, e is the electronic charge, n_H is the Hall carrier concentration, n is chemical carrier concentration, μ_H is the hall mobility, μ_0 is the carrier concentration independent mobility, m^* is density of state effective mass, L is Lorentz no and h is Planck's constant = 6.626 X 10^{-34} J-s. For the above calculation we have further assumed that the energy dependent relaxation time of carrier follows:

$$\tau = \tau_0 \left(\frac{E}{k_B T}\right)^{\lambda} \quad (8)$$

The parameter λ is called scattering parameter [1]. We have assumed $\lambda = -1/2$ corresponding to the combined effect of alloy scattering (AS) and acoustic phonon scattering (AP)[1],[25]. From the experimentally measured Seebeck coefficient and n_H, L, m^*, r_H etc. were calculated. Below we tabulate n_H, L, m^*, r_H (extracted from SPB model) and v_L (longitudinal velocity), v_T (transverse velocity), v_S (average sound velocity given by: $\frac{3}{v_S^3} = \frac{1}{v_L^3} + \frac{2}{v_T^3}$) measured using ultrasound technique, for all samples, at 300 K:

Sample	n_H**(/c.c.)**	r_H	L **(10^{-8} V^2/mK^2)**	m^*/m_e	μ_H **(cm^2/Vs)**	v_L **(m/s)**	v_T**(m/s)**	v_S**(m/s)**
S1	5.20×10^{18}	1.1723	1.50	2.04	87.93	5529	3390	3458
S2	2.96×10^{20}	1.0735	1.87	2.70	70.44	5269	3223	3290

Preprint not peer reviewed

This preprint research paper has not been peer reviewed. Electronic copy available at: https://ssrn.com/abstract=5179051

S3	2.67×10^{20}	1.0752	1.86	2.65	70.93	5283	3216	3284
S4	2.40×10^{20}	1.0878	1.80	2.55	90.8	5420	3114	3198
S5	1.65×10^{19}	1.1457	1.58	1.25	108.76	5543	3330	3404

For S1 and S5, SPB model is not much reliable as onset of bipolar conduction starts at much lower temperature due to their low n_H [20]. It is important to note that for sample S2, S3 and S4 m^* ~ 2.7 - 2.55m_e was observed throughout 300 K-660 K (also observed from fitting of Pisarenko plot) and it matches with the best reported m^* in the literature[20],[21],[37] for this type material. In addition to high m^*, these samples also exhibit excellent μ_H and to understand its origin we have plotted the temperature dependence of μ_H, which provides strong insight on underlying carrier scattering mechanism. From the Log [μ_H] vs Log [T] in Fig. 6. (a), we notice μ_H decreases slowly at low temperature followed by rather rapid decrease at high temperature. At low temperature follows $\mu_H \sim T^{-0.5}$ dependence suggesting alloy scattering (AS) contributes more to the overall Hall mobility and thus [20, 25, 37]. While at high temperature, acoustic phonon (AP) majorly dominates the charge transport behavior implying rapid decrease in mobility and leading to a temperature dependence of: $\mu_H \sim T^{-p}$ (p ~ 1-1.5) [1], [37]. In presence of both the AS and AP scatterings Matthiessen's rule apply as [20], [37]:

$$\frac{1}{\mu} = \frac{1}{\mu^{ph}} + \frac{1}{\mu^{alloy}} \tag{9}$$

Where drift mobility (μ) is related to Hall mobility (μ_H) via: $\mu = r_H \mu_H$. In SPB model the drift mobility due to AP scattering is expressed as:

$$\mu^{ph} = \frac{\sqrt{2}\pi e\hbar^4}{3(k_B T)^{\frac{3}{2}}} \frac{{v_L}^2 \rho}{{E_{def}}^2 (m_b^*)^{\frac{5}{2}}} \frac{F_0(\eta)}{F_{\frac{1}{2}}(\eta)} \tag{10}$$

Preprint not peer reviewed

This preprint research paper has not been peer reviewed. Electronic copy available at: https://ssrn.com/abstract=5179051

where v_L is longitudinal velocity of sound, ρ is the density of the material, ħ is reduced Planck's constant, E_{def} is the deformation potential that describes the strength of electron-phonon scattering and m_b^* is the average single valley effective mass related to density of state effective mass m^* via: $m^* = N_v^{\frac{2}{3}} m_b^*$. In the case for $Mg_2Si_{0.3}Sn_{0.7}$ band convergence produces $N_v = 6$ [20], [37]. In alloy or solid solution additional scattering mechanism i.e., scattering via fluctuation in potential due to atomic level disorder also contributes in limiting mobility. The drift mobility due to AS is expressed as:

$$\mu^{alloy} = \frac{16e\hbar^4}{9\sqrt{2}\pi x(1-x)(k_B T)^{\frac{1}{2}}} \frac{N_0}{E_{alloy}{}^2 (m_b^*)^{\frac{5}{2}}} \frac{F_0(\eta)}{F_{\frac{1}{2}}(\eta)} \qquad (11)$$

where N_0 is the no of atoms per unit volume, x (=0.7) is the fractional concentration of Sn in the solid solution and E_{alloy} is the alloy scattering potential. To understand the reason of high μ_H values, the temperature dependent drift mobility for S2, S3, S4 at different temperatures have been used to solve for the E_{def} and E_{alloy} and it has been found that a record low E_{def} ~ 8.0 - 8.1 eV and ultra-low alloy scattering potential E_{alloy} ~ 0.3 – 0.31 eV is responsible for the high mobility in our samples. It can be easily seen that the experimental values fit very nicely with the

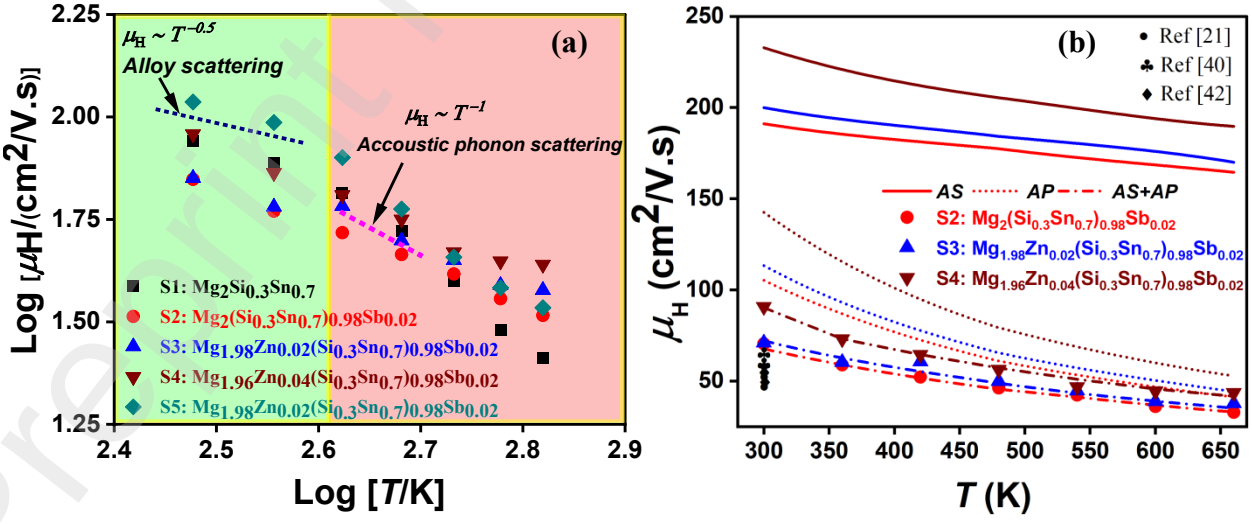

This preprint research paper has not been peer reviewed. Electronic copy available at: https://ssrn.com/abstract=5179051

Fig. 6. (a) Log [T] vs Log [μ_H] dependence and (b) μ_H vs T dependence of $Mg_{2(1-x)}Zn_{2x}(Si_{0.3}Sn_{0.7})_{1-y}Sb_y$ samples. The solid lines are plotted assuming carrier mobility is only limited by AS while dotted lines are plotted assuming only AP is present. The dotted-dashed lines represent when AS+AP combined effects are present [20].

theoretical AS+AP curves [Fig. 6. (b)]. Moreover, it can be noted that the Zn doped samples [Fig. 6. (a)] show lower AP scattering contribution towards mobility. It can also be observed that E_{def} and E_{alloy} for these samples are temperature independent as the mobility values fits nicely with the theoretical graphs generated at different temperatures using constant E_{def} and E_{alloy} potentials. It has been seen in literature that in different types of alloys like, n-type $Mg_2Si_{1-x}Sn_x$ [20], [37],[40], n-type $Si_{1-x}Ge_x$ [24, 41], $PbSe_{1-x}Te_x$ [24], [26], n-type $Gd_{1-x}Zn_xTe$ [42] values of E_{def} and E_{alloy} generally vary from 5-35 eV and 0.6-2.0 eV respectively. It should be mentioned that the record low E_{alloy} (~ 0.3 eV) in our samples indicate homogenous distribution of Si/Sn atoms in the alloy matrix resulting in zero band offset between the light and heavy conduction band edge and thus simultaneously ensuring high m^* as well as minimal inter band scattering lead reduction in mobility[37]. The negligible interband scattering [37] as well as inherent ultralow intraband scattering [43] simultaneously result in very high mobility and the proper band convergence ensures high m^* and Seebeck Coefficient.

Theoretical electronic structure:

It is well known that the primitive cell of Mg_2Si has an indirect band gap from Γ→X (Figure S9)[44]. The X point of the primitive cell folds onto the Γ point in the conventional cell making the principal band gap to appear direct at Γ point and similarly, the L point folds on to R point [Fig. 7(a)]. This kind of folding of high symmetry points of primitive cell onto other high symmetry points of non-primitive cells is common during electronic structure simulation[45], [46]. An underestimated band gap of 0.032 eV for Mg_2Si is typical of DFT based calculations due to

Preprint not peer reviewed

This preprint research paper has not been peer reviewed. Electronic copy available at: https://ssrn.com/abstract=5179051

the considered approximations[5]. The partial density of states (pDOS) reveals that Si 'p' states form the valence band while 's' states of Mg have dominant contribution in the conduction band [Fig. 7(b)][47]. When Sn atoms replaced some of the Si atoms in $Mg_2Si_{0.3}Sn_{0.7}$ still preserving the original crystal structure, we see that the band gap vanishes in the electronic structure leading to the onset of bipolar effect in the samples as observed experimentally [Fig. 7(c)]. The notable feature in the electronic structure is the onset of convergence of bands at R point.

Preprint not peer reviewed

This preprint research paper has not been peer reviewed. Electronic copy available at: https://ssrn.com/abstract=5179051

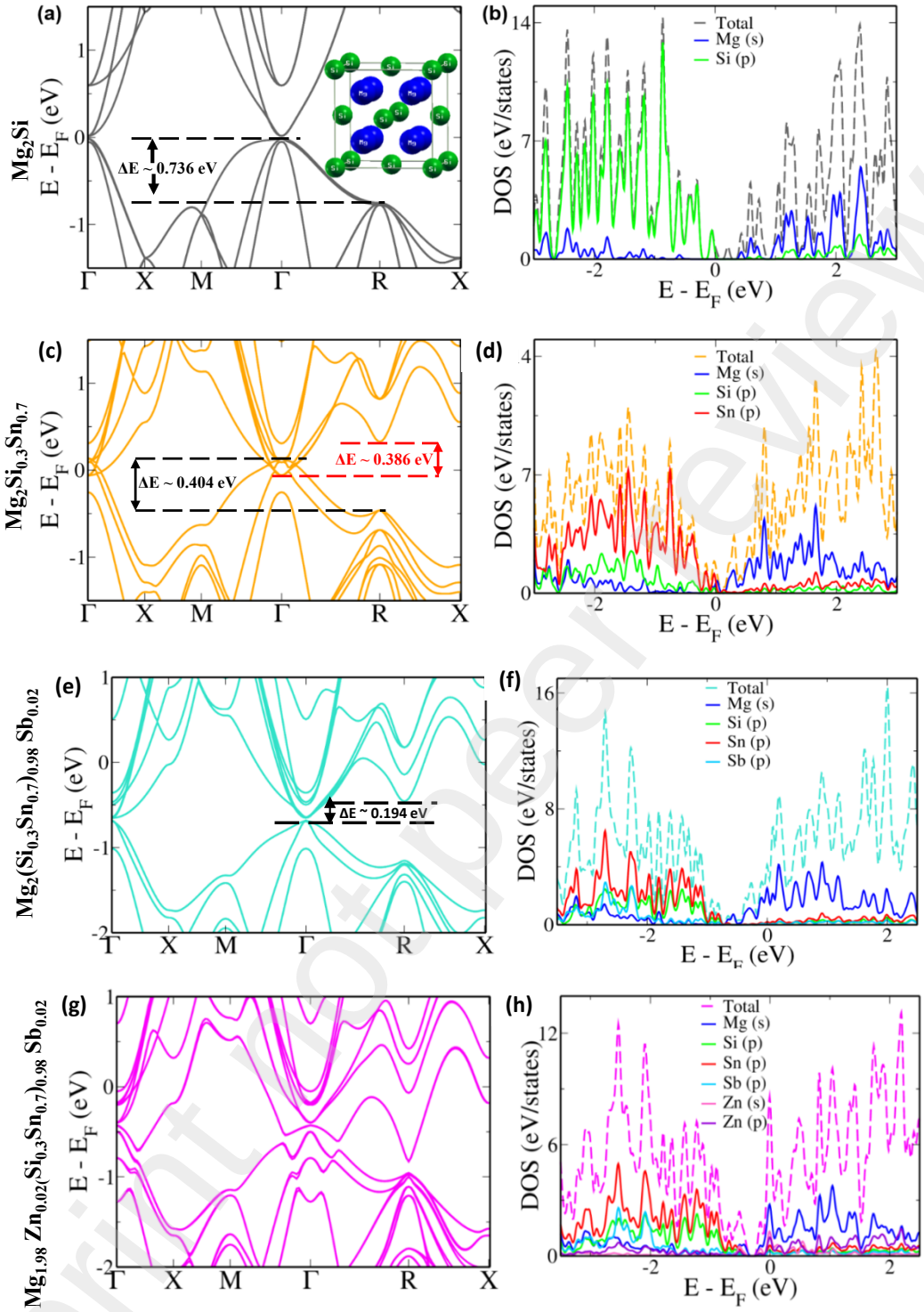

Figure 7. Electronic structure and pDOS of (a, b) Mg_2Si (c, d) $Mg_2Si_{0.3}Sn_{0.7}$ (e, f) Sb doped $Mg_2Si_{0.3}Sn_{0.7}$ (g, h) Sb and Zn co-doped $Mg_2Si_{0.3}Sn_{0.7}$.

While Mg_2Si had ΔE of 0.736 eV and 1.747 eV, respectively in the valence and conduction band region between Γ point and R point, in $Mg_2Si_{0.3}Sn_{0.7}$ it reduces drastically to 0.404 eV and 0.386

This preprint research paper has not been peer reviewed. Electronic copy available at: https://ssrn.com/abstract=5179051

eV respectively (Fig. 7(d)). This additional contribution from valleys at R point in addition to that at Γ point helps in increasing the effective mass m^* by increasing N_v[48]. The p-DOS reveals 'p' states of Si and Sn in the valence band region and 's' states of Mg in the conduction band region [Fig. 7(d)]. This pattern remains the same even in the case of supercell of twice the size. [Supplementary file: Fig. S10]. The electronic structure of Sb doped $Mg_2Si_{0.3}Sn_{0.7}$ reveals the increase in the band gap at Γ point to 0.03 eV which helps to counter the bipolar effect in the samples [Fig. 7(e)]. The ΔE values reduces to 0.194 eV in the conduction band region leading to further increase in the m^* values as observed experimentally due to increase in N_v[48]. The contribution of 'p' states of Sb is seen in the valence band region in the pDOS plot [Fig. 7(f)]. Hence, in addition to tuning the carrier concentration Sb doping improves the effective mass of carrier the sample. It is very interesting to note that the co-doping of Zn along with Sb in $Mg_2Si_{0.3}Sn_{0.7}$ shows a unique electronic structure [Fig. 7(g)]. The band gap is further seen to increase to 0.072 eV leading to elimination of bipolar effect. The conduction band edge shows pudding mold band structure with a flat portion around Γ point (responsible for enhanced m^*) and a dispersive portion[49], [12]. Further, the band at R point shows hyper-convergence of 0.402 eV with pointy edge at the end. These features lead to increased mobility of the carriers and slight decrease in m^* with increase in Zn concentration. Further, the valence band edge shows generation of multiple electron valleys beneficial for p-type conduction[50]. The pDOS reveals hybridization of Zn 's' and 'p' states with 's' states of Mg leading to the formation of pudding mold band structure (Fig 7(h)). When Mg vacancies are introduced (sample S5) the band gap again closes leading to onset of bipolar conduction [Supplementary file:Figure S11][51]. The divergence of the band at R point possibly leads to decrease in the m^* observed experimentally.

Thermal conductivity and Figure of merit *ZT*:

Preprint not peer reviewed

This preprint research paper has not been peer reviewed. Electronic copy available at: https://ssrn.com/abstract=5179051

The temperature dependence of κ_{total} vs T is plotted in Fig. 8 (a). The sample S1 being undoped shows decreasing κ_{total} up to ~ 450 K followed by an increasing trend due onset of bipolar conduction. As shown earlier the Sb doping tunes the carrier concentration in S2, S3, S4 samples making these degenerate in nature and κ_{total} showing decreasing trend with T. In S5, vacancies at Mg sites again make the sample bipolar in nature thus showing an upturn of κ_{total} above 525 K. It can be seen from the Figure 2 (b, c) that the Seebeck coefficient and electrical conductivity remains appreciably same for S2, S3 and S4. The 2 atomic % Zn doped S4: $Mg_{1.96}Zn_{0.04}(Si_{0.3}Sn_{0.7})_{0.98}Sb_{0.02}$ sample shows lowest κ_{total} among all degenerate samples. The high power factor along with lowest κ_{total} results in a high ZT_{max} ~ 1.55 at 673 K for S4: $Mg_{1.96}Zn_{0.04}(Si_{0.3}Sn_{0.7})_{0.98}Sb_{0.02}$ sample, which is close to best reported value for this material [21], [22]. Finally, $\kappa_{lattice}+\kappa_{bipolar}$ is calculated by subtracting the electronic part of thermal conductivity ($\kappa_{electronic} = L\sigma T$) from κ_{total} and plotted in Fig. 8 (b). From the arrow drawn in Fig. 8 (b), it is seen that for all samples $\kappa_{lattice}$ shows $T^{-0.5}$ dependence rather than T^{-1} in the low temperature range where $\kappa_{bipolar}$ is negligible. This is due to the dominant phonon scattering through the alloying induced point defect scattering of phonons rather than Umklapp scattering,($\kappa_{lattice} \sim T^{-1}$) [20], [37].

Preprint not peer reviewed

This preprint research paper has not been peer reviewed. Electronic copy available at: https://ssrn.com/abstract=5179051

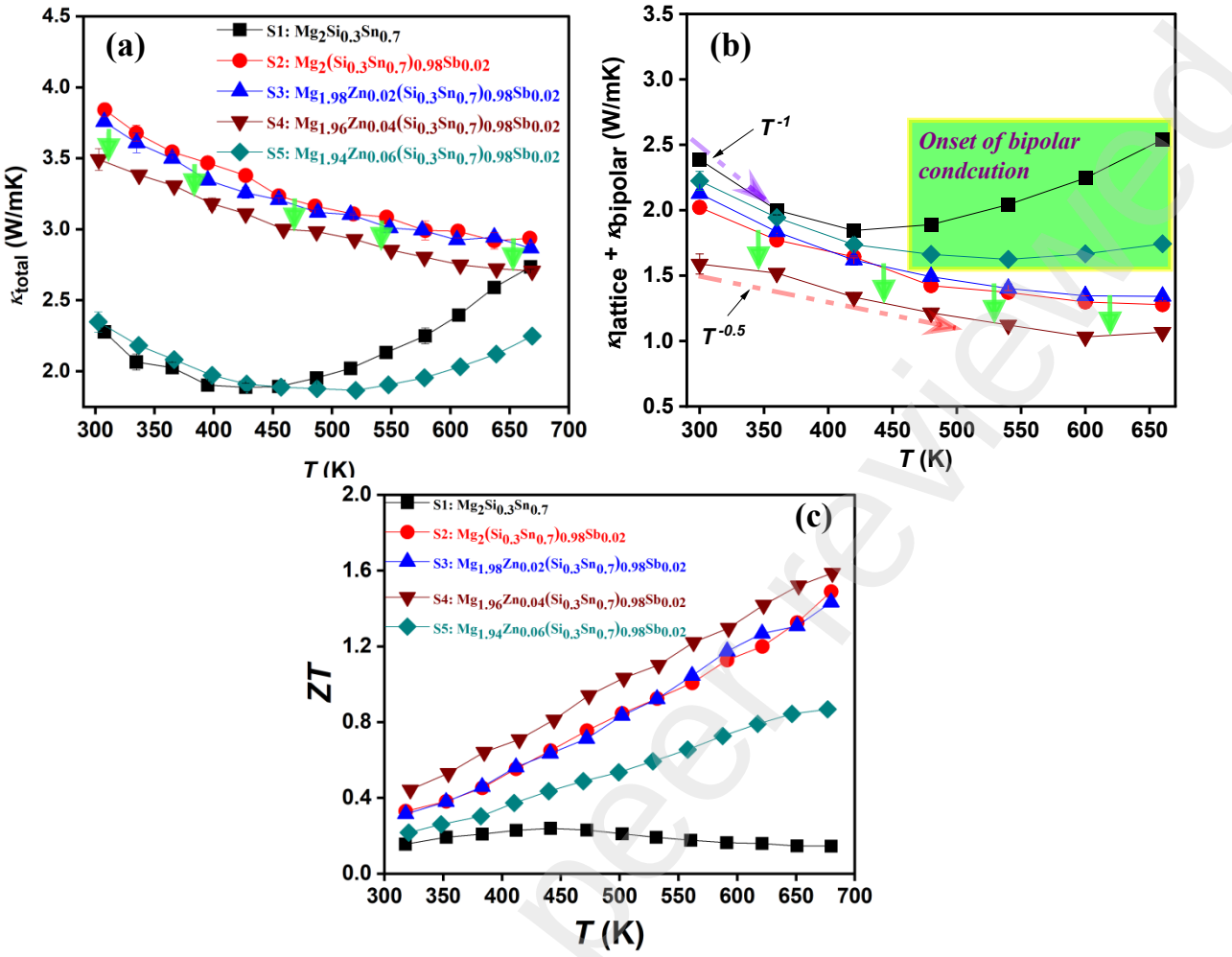

Fig. 8. Temperature dependence of (a) κ_{total}, (b) $\kappa_{lattice}$+$\kappa_{bipolar}$, (c) *ZT*

With Zn doping, κ_{total} decreases in S3 and S4 compared to S2. The Zn substitutions at Mg site bring further mass and size mismatch, introducing strain in the lattice. In Fig. 8 (b). we see that out of all degenerate samples, S4 shows lowest $\kappa_{lattice}$+$\kappa_{bipolar}$. Moreover, in sample S4 we notice decrease of ~ 25% in $\kappa_{lattice}$+$\kappa_{bipolar}$ compared to S2 at 300 K and ~ 18-20% at high temperature up-to 673 K, which is generally due to scattering of short to mid-wavelength phonons (~ 3 -100 nm)[21],[52],[53]. To further understand the origin of lowering of κ_{total}, morphology of the sample was studied using TEM. From the TEM images shown in Fig. 9 (a) we see Moiré Pattern formed which generally happens when there is a slight lattice mismatch (~ 0.01 Å) among two different regions of lattice, which is possible as Zn doped and undoped regions can have slightly different

Preprint not peer reviewed

This preprint research paper has not been peer reviewed. Electronic copy available at: https://ssrn.com/abstract=5179051

lattice parameters[54], [55]. From the marked region in Fig. 9 (a). FFT was generated and shown in inset of 9 (a). where we see different dots (marked in red and white arrows) representing slightly different lattice parameters. Using these dots IFFT images shown in Fig. 12. (b) and (c) were generated respectively. In Fig. 9 (b) we see lattice plane without dislocations. However, Fig. 9 (c) reveals dense network of dislocations (marked with red) gathered around in a region of lateral dimension of ~ 20/30 nm. These two planes with slightly different lattice parameters could generate the Moiré Pattern. These were further analyzed via geometric phase analysis (GPA) [56], [57], a semi-quantitative lattice image-processing approach that can reveal spatial distribution of strain fields. The GPA combines both the real-space and reciprocal-space information where the displacements are measured by calculating 'local' Fourier components of the lattice fringes in an image [56]. Fig. 9 (d)-(e) show the analyzed GPA results of Fig. 10 (c), namely the component ε_{xy} and ω_{xy} of the strain. The strain mapping[58] shows strain regions comprising of the dislocation core and elastic stress field around it of dimension ~ 10-15 nm. These extra high density of dislocations embedded in the in the grains, randomly distributed dislocations along with the local strain accumulation contributes strongly in scattering low and mid frequency phonons [21], [52]. The significant reduction in $\kappa_{lattice}$ due to lattice strains and mass mismatch acts as phonon scatterers, thus reducing total thermal conductivity (~10%) compared to Zn un-doped samples in the entire temperature range (300-673 K).

Preprint not peer reviewed

This preprint research paper has not been peer reviewed. Electronic copy available at: https://ssrn.com/abstract=5179051

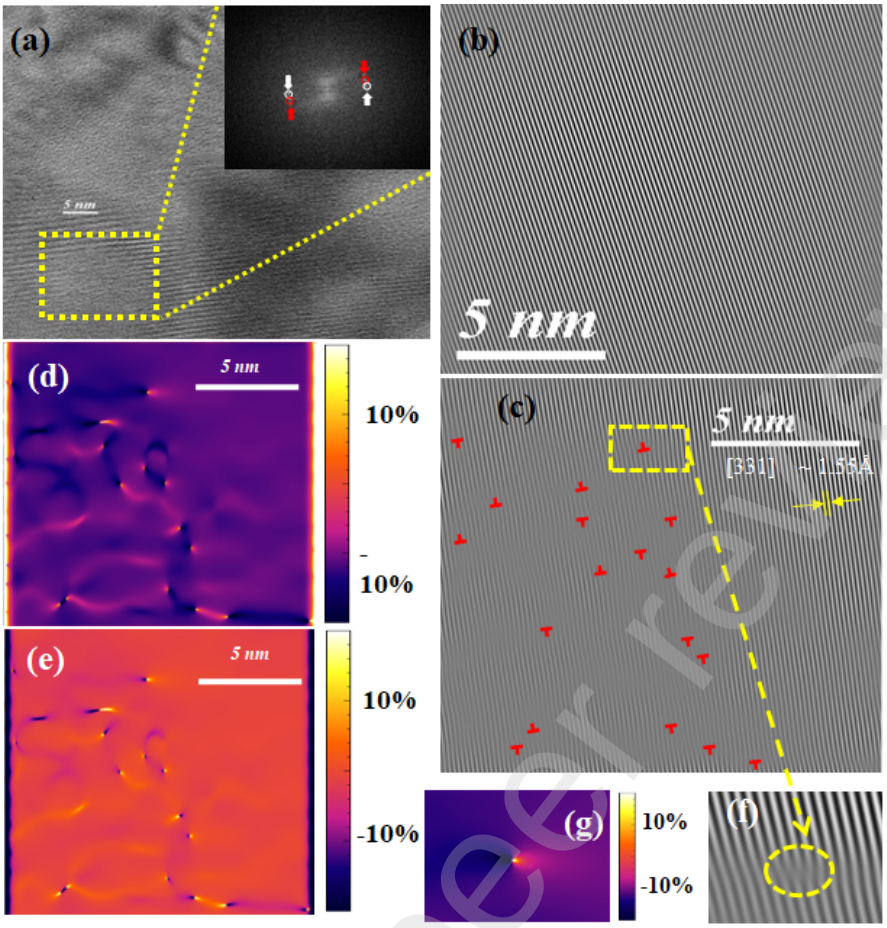

Fig.9. (a) HRTEM of S4. The region marked with yellow dashed square shows Moiré pattern. Inset shows the FFT of the mentioned region, showing different (red and white colored) dots in FFT representing regions with slightly different lattice parameters, (b) Using the diffraction marks marked with red and white arrows, Inverse FFT is done and IFFT images (b) and (c) are generated respectively. (c) Dislocations are marked with red colour in. (d) strain mapping in the xy direction (ε_{xy}) (e) and rotation tensor (ω_{xy}) is color mapped using strain++ software via GPA (Geometric Phase Analysis). (f) An enlarged dislocation core and (g) strain (ε_{xy}) tensor around it plotted with high intensity.

Fabrication of uni-leg device and evaluation of its efficiency:

To estimate the electrical power generation capability engineering figure-of-merit $(ZT)_{eng}$ and efficiency (η_{max}) were estimated for the optimized $Mg_{1.96}Zn_{0.04}(Si_{0.3}Sn_{0.7})_{0.98}Sb_{0.02}$ assuming cold end temperature T_c = 328 K. The $(ZT)_{eng}$ and η_{max} is defined as follows[59]:

This preprint research paper has not been peer reviewed. Electronic copy available at: https://ssrn.com/abstract=5179051

$$(ZT)_{eng} = \frac{(\int_{T_c}^{T_h} \alpha(T)dT)^2 \Delta T}{(\int_{T_c}^{T_h} \rho(T)dT)(\int_{T_c}^{T_h} \kappa\text{total}(T)dT)} \quad (12)$$

$$\eta_{max} = \eta_{max} \frac{(\sqrt{1 + (ZT)_{eng}(\hat{\alpha}/\eta_c - 1/2)} - 1)\Delta T}{\hat{\alpha}\left(\sqrt{1 + (ZT)_{eng}\left(\hat{\alpha}/\eta_c - 1/2\right)} + 1\right) - \eta_c} \quad (13)$$

$$\Delta T = T_h - T_c \quad (14)$$

$$\hat{\alpha} = \frac{\alpha(T_h)\Delta T}{\int_{T_c}^{T_h} \alpha(T)dT} \quad (15)$$

Where $\alpha(T,)$ $\rho(T)$, $\kappa_{total}(T)$, η_C, and $\hat{\alpha}$ represent temperature dependent Seebeck coefficient, electrical resistivity, thermal conductivity, Carnot efficiency and a dimensionless intensity factor of Thomson coefficient respectively.

The maximum ZT_{eng} of $Mg_{1.96}Zn_{0.04}(Si_{0.3}Sn_{0.7})_{0.98}Sb_{0.02}$ is found to be ~0.69 where the highest η_{max} is determined as ~12% for ΔT of 382 K (T_h ~ 675 K, details given in Fig. 10(a)). Finally, a uni-leg $Mg_{1.96}Zn_{0.04}(Si_{0.3}Sn_{0.7})_{0.98}Sb_{0.02}$ with metallized (Ag) ends was fabricated using monobloc sintering process as shown in Fig. 10(b). For making electrical connections Ag sheet of thickness ~ 150μm were soldered to the thermoelement using high temperature solder. The current-voltage characteristics and the output power of the uni-leg device (at a ΔT of 329 K) are shown in Figure 10(C). The open circuit voltage (V_{oc}) of the uni-leg device was found to be ~ 41 mV and at a load resistance (R_L) of ~ 0.7 mΩ the maximum output power of ~505 mW was obtained (Fig. 10(c)). From the V_{oc} value and electrical output measured at load resistance of 0.7 mΩ the total internal resistance of the uni-leg device was found to be (R_{in}) ~ 0.6 mΩ. At matched load of 0.6 mΩ the maximum electrical output power (*Pmax*) produced by the uni-device can be

Preprint not peer reviewed

This preprint research paper has not been peer reviewed. Electronic copy available at: https://ssrn.com/abstract=5179051

estimated using relation: $V_{OC}^2/4\ R_{in}$ and it was found to be 700 mW. The measured experimental conversion efficiency (η_{max}) of this uni-leg device is estimated by taking the ratio of electrical output power (P_{max}) to heat flowing (Q_H ~ 7W) across the uni-leg and the experimental η of ~ 9.5 % was obtained for ΔT = 329 K at matched load of ~ 0.6 mΩ. The $\eta_{\max}$ calculated using $(ZT)_{eng}$ was found to be ~ 11.2% at ΔT = 329 K (T_h~ 657 K). The loss of efficiency by 15 % in experimental device is attributed to the loss of power at contact resistance between the active thermoelectric materials and various other interfaces including Ag electrode present in the uni-leg device. The specific contact resistivity (ρ_C) was estimated as per the approach described in our previous publications and the value of ρ_C was found to be 63 μΩ-cm^2 [60]. The contribution of total contact resistance (~0.1 mΩ) to total uni-leg device resistance (~ 0.6 mΩ) is found to be 17%, which is close to the above estimated efficiency loss. For an efficient thermoelectric power generator the acceptable value of specific electrical contact resistance should be < 100 μΩcm^2 [19a].

Preprint not peer reviewed

This preprint research paper has not been peer reviewed. Electronic copy available at: https://ssrn.com/abstract=5179051

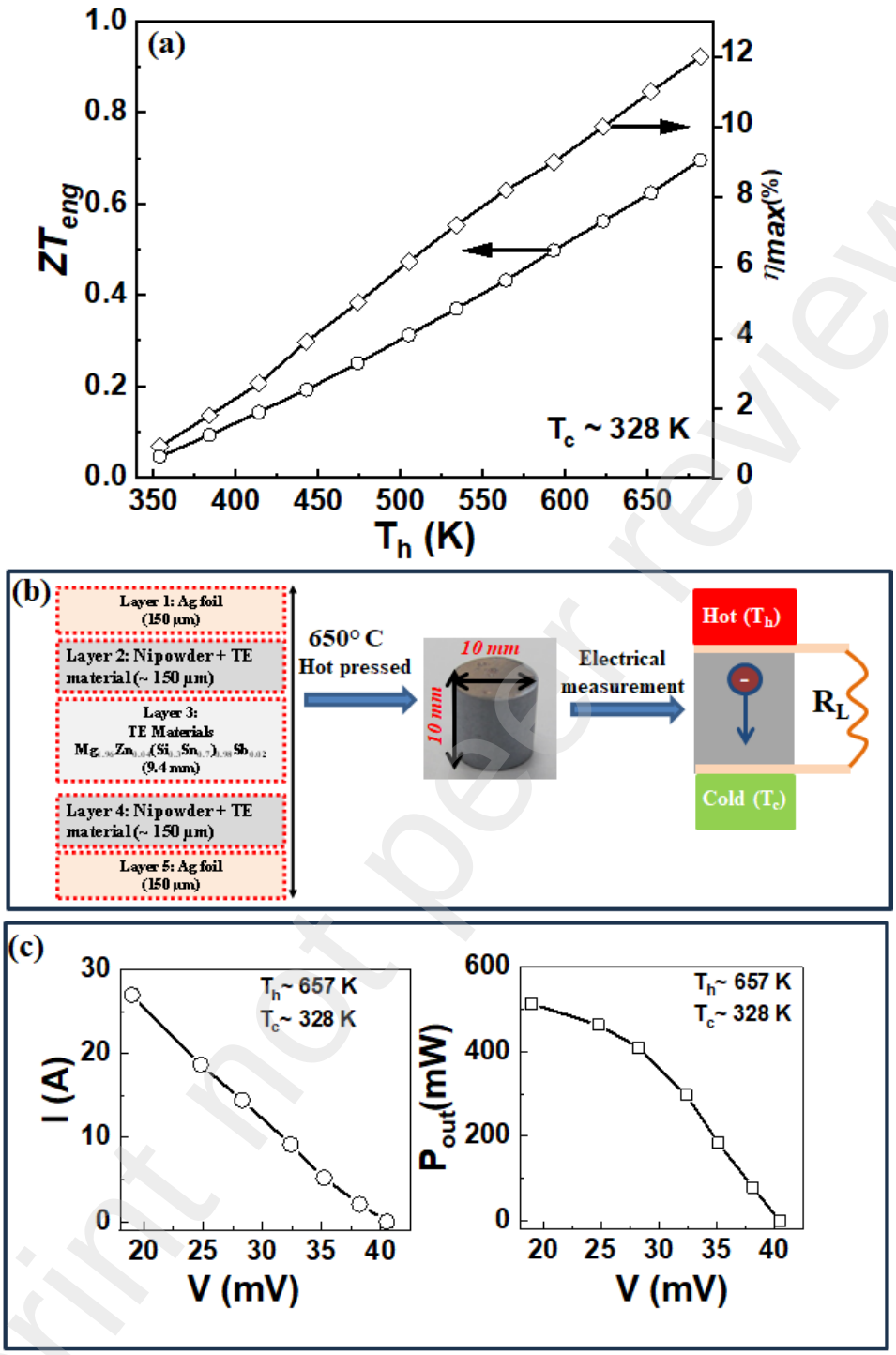

Figure 10: (b) Schematic showing monolithic sintering of the $Mg_{1.96}Zn_{0.04}(Si_{0.3}Sn_{0.7})_{0.98}Sb_{0.02}$ along with Ni buffer layers and metallic (Ag) contact layer at the ends. Inset shows the photograph of the pellet and electrical output characteristics of the $Mg_{1.96}Zn_{0.04}(Si_{0.3}Sn_{0.7})_{0.98}Sb_{0.02}$ uni-leg device at ΔT~ 329 K.

This preprint research paper has not been peer reviewed. Electronic copy available at: https://ssrn.com/abstract=5179051

Conclusions:

In this work, we demonstrate that the controlled synthesis of the $Mg_2Si_{0.3}Sn_{0.7}$ samples leads to the homogenous distribution of Si/Sn atoms with negligible presence of MgO. The improved Hall mobility in our samples are due to reduced inter and intra band scattering expressed by record low E_{def} (8.0 - 8.1 eV) and E_{alloy} (0.3 - 0.31 eV) potentials. The Sb doping helps in reducing the $\kappa_{lattice\ and}$ optimizing the carrier concentration. With the help of DFT calculations, we explicitly showed that dopant atoms can change the effective mass of carriers in the $Mg_2Si_{0.3}Sn_{0.7}$ from $2.0m_e$ to $\sim 2.6m_e$ thus demonstrating a little departure from SPB model in the doped samples and confirmed experimentally. We further demonstrate that the Zn doping (up to 2 atomic %) at Mg site changes the band structure by introducing hyper convergence at the R point of Brillouin Zone, thus increasing the charge carrier mobility further up to 90 $cm^2/V.s$. In addition, the Zn substitution at Mg sites introduces high density of dislocations embedded in the in the grains of Zn, Sb co-doped $Mg_2Si_{0.3}Sn_{0.7}$ samples. These randomly distributed dislocations along with the local strain accumulation contributes in scattering of low and mid frequency phonons thus further decreasing $\kappa_{lattice}$ by ~ 20% over whole temperature range (300-673 K). The overall synergetic balance of electrical and thermal transport via Sb and Zn doping resulted in a very high ZT ~1.6 (at 673 K) in $Mg_{1.96}Zn_{0.04}(Si_{0.3}Sn_{0.7})_{0.98}Sb_{0.02}$ close to the best reported value. Further proof of high ZT is witnessed through the realization of impressive high efficiency of 9.5 % at ΔT~ 329 K in the uni-leg device of $Mg_{1.96}Zn_{0.04}(Si_{0.3}Sn_{0.7})_{0.98}Sb_{0.02}$.

Acknowledgement: We sincerely thank Professor Titas Dasgupta from MEMS I.I.T Bombay regarding his inputs provided for the optimization of the synthesis procedure of doped & undoped Magnesium Silicides samples.

Preprint not peer reviewed

This preprint research paper has not been peer reviewed. Electronic copy available at: https://ssrn.com/abstract=5179051

References

[1] A. F. May, G. J. Snyder, *Materials, preparation, and characterization in thermoelectrics* **2012**, 1-18.

[2] J. Mao, Z. Liu, J. Zhou, H. Zhu, Q. Zhang, G. Chen, Z. Ren, *Advances in Physics* **2018**, *67*, 69-147.

[3] U. S. Shenoy, K. D. Goutham, D. K. Bhat, *Materials Advances* **2022**, *3*, 5941-5946.

[4] J. P. Heremans, B. Wiendlocha, A. M. Chamoire, *Energy & Environmental Science* **2012**, *5*, 5510-5530.

[5] D. K. Bhat, U. S. Shenoy, *Materials Today Physics* **2019**, *11*, 100158.

[6] Z. Z. Luo, S. Cai, S. Hao, T. P. Bailey, I. Spanopoulos, Y. Luo, J. Xu, C. Uher, C. Wolverton, V. P. Dravid, *Angewandte Chemie International Edition* **2021**, *60*, 268-273.

[7] J. P. Heremans, V. Jovovic, E. S. Toberer, A. Saramat, K. Kurosaki, A. Charoenphakdee, S. Yamanaka, G. J. Snyder, *Science* **2008**, *321*, 554-557.

[8] Q. Zhang, Z. Ti, Y. Zhu, Y. Zhang, Y. Cao, S. Li, M. Wang, D. Li, B. Zou, Y. Hou, *ACS nano* **2021**, *15*, 19345-19356.

[9] Y. Pei, H. Wang, G. J. Snyder, *Advanced materials* **2012**, *24*, 6125-6135.

[10] W. Liu, X. Tan, K. Yin, H. Liu, X. Tang, J. Shi, Q. Zhang, C. Uher, *Physical review letters* **2012**, *108*, 166601.

[11] U. S. Shenoy, K. D. Goutham, D. K. Bhat, *Journal of Alloys and Compounds* **2022**, *905*, 164146.

[12] K. Mori, H. Sakakibara, H. Usui, K. Kuroki, *Physical Review B—Condensed Matter and Materials Physics* **2013**, *88*, 075141.

[13] E. B. Isaacs, C. Wolverton, *Physical Review Materials* **2019**, *3*, 015403.

[14] U. S. Shenoy, D. K. Bhat, *ACS Sustainable Chemistry & Engineering* **2021**, *9*, 13033-13038.

[15] C. Zhao, Z. Li, T. Fan, C. Xiao, Y. Xie, *Research* **2020**.

[16] K. Kōmoto, T. Mori, *Thermoelectric Nanomaterials: Materials Design and Applications*, Springer, **2013**.

[17] J. Bardeen, W. Shockley, *Physical review* **1950**, *80*, 72.

[18] G. A. Slack, D. M. Rowe, *Edition. Rowe DM. Chemical Rubber company. Boca Raton* **1995**, *407*.

Preprint not peer reviewed

This preprint research paper has not been peer reviewed. Electronic copy available at: https://ssrn.com/abstract=5179051

[19] a)D. M. Rowe, *CRC handbook of thermoelectrics*, CRC press, **2018**; b)G. Jiang, J. He, T. Zhu, C. Fu, X. Liu, L. Hu, X. Zhao, *Advanced Functional Materials* **2014**, *24*, 3776-3781.

[20] X. Liu, T. Zhu, H. Wang, L. Hu, H. Xie, G. Jiang, G. J. Snyder, X. Zhao, *Advanced Energy Materials* **2013**, *3*, 1238-1244.

[21] G. K. Goyal, S. Mukherjee, R. C. Mallik, S. Vitta, I. Samajdar, T. Dasgupta, *ACS Applied Energy Materials* **2019**, *2*, 2129-2137.

[22] B. Wang, H. Zhao, J. Li, B. Zhang, D. Wang, C. Chen, A. Song, W. Hu, D. Yu, B. Xu, *Journal of Materiomics* **2024**, *10*, 285-292.

[23] a)J. Callaway, H. C. von Baeyer, *Physical Review* **1960**, *120*, 1149; b)P. G. Klemens, *Physical review* **1960**, *119*, 507.

[24] H. Wang, A. D. LaLonde, Y. Pei, G. J. Snyder, *Advanced Functional Materials* **2013**, *23*, 1586-1596.

[25] H. Kamila, P. Sahu, A. Sankhla, M. Yasseri, H.-N. Pham, T. Dasgupta, E. Mueller, J. de Boor, *Journal of Materials Chemistry A* **2019**, *7*, 1045-1054.

[26] H. Wang, Y. Pei, A. D. LaLonde, G. J. Snyder, *Proceedings of the National Academy of Sciences* **2012**, *109*, 9705-9709.

[27] H. Gao, T. Zhu, X. Zhao, Y. Deng, *Dalton Transactions* **2014**, *43*, 14072-14078.

[28] J. Zhao, Z. Liu, J. Reid, K. Takarabe, T. Iida, B. Wang, U. Yoshiya, S. T. John, *Journal of Materials Chemistry A* **2015**, *3*, 19774-19782.

[29] P. Giannozzi, S. Baroni, N. Bonini, M. Calandra, R. Car, C. Cavazzoni, D. Ceresoli, G. L. Chiarotti, M. Cococcioni, I. Dabo, *Journal of physics: Condensed matter* **2009**, *21*, 395502.

[30] J. P. Perdew, K. Burke, M. Ernzerhof, *Physical review letters* **1996**, *77*, 3865.

[31] J. De Boor, T. Dasgupta, H. Kolb, C. Compere, K. Kelm, E. Mueller, *Acta Materialia* **2014**, *77*, 68-75.

[32] a)J. de Boor, S. Gupta, H. Kolb, T. Dasgupta, E. Müller, *Journal of Materials Chemistry C* **2015**, *3*, 10467-10475; b)Z. Ren, Y. Lan, Q. Zhang, *Advanced thermoelectrics: materials, contacts, devices, and systems*, CRC Press, **2017**.

[33] T. Dasgupta, C. Stiewe, J. de Boor, E. Müller, *physica status solidi (a)* **2014**, *211*, 1250-1254.

[34] W. Liu, Q. Zhang, K. Yin, H. Chi, X. Zhou, X. Tang, C. Uher, *Journal of Solid State Chemistry* **2013**, *203*, 333-339.

Preprint not peer reviewed

This preprint research paper has not been peer reviewed. Electronic copy available at: https://ssrn.com/abstract=5179051

[35] B. Klobes, J. de Boor, A. Alatas, M. Y. Hu, R. E. Simon, R. P. Hermann, *Physical review materials* **2019**, *3*, 025404.

[36] Z. Du, T. Zhu, Y. Chen, J. He, H. Gao, G. Jiang, T. M. Tritt, X. Zhao, *Journal of Materials Chemistry* **2012**, *22*, 6838-6844.

[37] W. Liu, H. Chi, H. Sun, Q. Zhang, K. Yin, X. Tang, Q. Zhang, C. Uher, *Physical Chemistry Chemical Physics* **2014**, *16*, 6893-6897.

[38] a)H. Gao, T. Zhu, X. Liu, L. Chen, X. Zhao, *Journal of Materials Chemistry* **2011**, *21*, 5933-5937; b)W. Liu, X. Tang, H. Li, J. Sharp, X. Zhou, C. Uher, *Chemistry of Materials* **2011**, *23*, 5256-5263; c)W. Liu, X. Tang, J. Sharp, *Journal of Physics D: Applied Physics* **2010**, *43*, 085406; d)J. Chen, W. Xue, S. Li, G. Zhang, G. Cai, H. Zhao, *RSC advances* **2019**, *9*, 4008-4014.

[39] H. Kamila, A. Sankhla, M. Yasseri, E. Mueller, J. de Boor, *Advanced Science* **2020**, *7*, 2000070.

[40] L. D. Crossman, G. C. Danielson, *Physical Review* **1968**, *171*, 867.

[41] S. Krishnamurthy, A. Sher, A.-B. Chen, *Applied Physics Letters* **1985**, *47*, 160-162.

[42] D. Chattopadhyay, *Solid state communications* **1994**, *91*, 149-151.

[43] M. I. Fedorov, D. A. Pshenay-Severin, V. K. Zaitsev, S. Sano, M. V. Vedernikov, IEEE, pp. 142-145.

[44] Y. Li, T. Ma, Y. Ren, T. Liu, X. Zou, *Materials Research Express* **2020**, *7*, 036533.

[45] U. S. Shenoy, D. K. Bhat, *Journal of Physics and Chemistry of Solids* **2024**, *188*, 111943.

[46] U. S. Shenoy, D. K. Bhat, *Energy Advances* **2022**, *1*, 15-20.

[47] P. Boulet, M. J. Verstraete, J. P. Crocombette, M. Briki, M. C. Record, *Computational Materials Science* **2011**, *50*, 847-851.

[48] U. S. Shenoy, D. K. Bhat, *Journal of Alloys and Compounds Communications* **2024**, *1*, 100001.

[49] K. Kuroki, R. Arita, *Journal of the Physical Society of Japan* **2007**, *76*, 083707-083707.

[50] U. S. Shenoy, D. K. Bhat, *Journal of Alloys and Compounds* **2021**, *872*, 159681.

[51] U. S. Shenoy, D. K. Bhat, *Materials Advances* **2021**, *2*, 6267-6271.

[52] K. Biswas, J. He, I. D. Blum, C.-I. Wu, T. P. Hogan, D. N. Seidman, V. P. Dravid, M. G. Kanatzidis, *Nature* **2012**, *489*, 414-418.

[53] Z. Liu, J. Mao, T.-H. Liu, G. Chen, Z. Ren, *Mrs Bulletin* **2018**, *43*, 181-186.

[54] W. Saito, K. Hayashi, J. Dong, J.-F. Li, Y. Miyazaki, *Scientific reports* **2020**, *10*, 2020.

Preprint not peer reviewed

This preprint research paper has not been peer reviewed. Electronic copy available at: https://ssrn.com/abstract=5179051

[55] S. Acharya, J. Hwang, K. Kim, J. Kim, W. Hwang, A. Soon, W. Kim, *Nano Energy* **2023**, *112*, 108493.

[56] M. J. Hÿtch, E. Snoeck, R. Kilaas, *Ultramicroscopy* **1998**, *74*, 131-146.

[57] Z. Liu, Y. Wang, J. Mao, H. Geng, J. Shuai, Y. Wang, R. He, W. Cai, J. Sui, Z. Ren, *Advanced Energy Materials* **2016**, *6*, 1502269.

[58] S. Kumar, M. Tiadi, V. Trivedi, M. Battabyal, D. K. Satapathy, *ACS Applied Energy Materials* **2023**, *6*, 10457-10466.

[59] H. S. Kim, W. Liu, G. Chen, C.-W. Chu, Z. Ren, *Proceedings of the National Academy of Sciences* **2015**, *112*, 8205-8210.

[60] A. Singh, S. Bhattacharya, C. Thinaharan, D. K. Aswal, S. K. Gupta, J. V. Yakhmi, K. Bhanumurthy, *Journal of Physics D: Applied Physics* **2008**, *42*, 015502.

Preprint not peer reviewed

This preprint research paper has not been peer reviewed. Electronic copy available at: https://ssrn.com/abstract=5179051